# Characterization and Modeling of Heterogeneous Deformation in Commercial Purity Titanium

**Y. Yang, L. Wang, C. Zambaldi, P. Eisenlohr, R. Barabash, W. Liu, M.R. Stoudt, M.A. Crimp, and T.R. Bieler**

*Heterogeneous deformation, including local dislocation shear activity and lattice rotation, was analyzed in microstructure patches of polycrystalline commercial purity titanium specimens using three different experimental methods. The measurements were compared with crystal plasticity finite element simulations for the same region that incorporate a local phenomenological hardening constitutive model. The dislocation activity was measured using techniques associated with atomic force microscopy, confocal microscopy, three-dimensional x-ray diffraction, and nano-indentation. The results indicate that a major challenge for model development is to effectively predict conditions where slip transfer occurs, and where geometrically necessary dislocations accumulate.*

## INTRODUCTION

Titanium and its alloys are widely used because of their high stiffness, strength, and corrosion resistance. However, the processes of heterogeneous plastic deformation and fracture initiation in hexagonal α-titanium are still not well understood. Heterogeneous deformation usually results from two phenomena.[1–3] One is that some grains are much more easily deformed than other grains, because one or more deformation systems in the "soft" grains can be more easily activated than those in "hard" grains under an imposed stress state, leading to large strain differences among soft and hard grains. The other aspect is the heterogeneous deformation associated with strain gradients within a given grain, resulting from the requirement for local arbitrary grain shape changes needed to achieve polycrystalline compatibility.

A prominent feature of the plastic deformation of hexagonal α-titanium is the plastic anisotropy arising from four types of dislocation slip systems with various critical resolved shear stresses (CRSS).[4,5] The primary slip system is $\{10\bar{1}0\}<1\bar{2}10>$ prismatic slip because it has the lowest critical resolved shear stress.[4] There are three other slip systems, $\{0001\}<1\bar{2}10>$ basal, $\{10\bar{1}1\}<\bar{1}2\bar{1}0>$ pyramidal <a> slip, and $\{10\bar{1}1\}<2\bar{1}\bar{1}\bar{3}>$ pyramidal <c+a> slip, that can be activated with high resolved shear stress. There are also four twinning systems in α-titanium[6] that can contribute to deformation, two tensile (extension) twinning modes (T1 and T2), and two compressive (contraction) twinning modes (C1 and C2). During tensile tests at room temperature, $\{10\bar{1}2\}<\bar{1}011>$ T1 twinning is commonly observed, in part due to its relatively low magnitude of shear.[6]

The crystal plasticity finite element (CPFE) method is often used to simulate the three-dimensional (3D) plastic deformation processes in polycrystalline materials, because heterogeneous deformation between and within grains can be simulated.[7–10] Crystal plasticity finite element modeling incorporates the crystallographic nature of dislocation slip into the finite element method by assuming that the plastic velocity gradient is composed of the shear contributions of all slip systems.[11,12] Simulation of grain patches using the CPFE method, however, are not always able to match experimental observations.[12,13]

To further understand and eventually better simulate the heterogeneous deformation processes in polycrystalline α-titanium, this research project is focused on both detailed experimental characterization and the CPFE modeling of heterogeneous deformation using a phenomenological CPFE constitutive model. Several experimental characterization techniques, including atomic force microscopy (AFM), confocal microscopy, three-dimensional x-ray diffraction (3D-XRD), and nano-indentation, were used to quantitatively measure the active deformation systems in grains with different orientations. The critical resolved shear stresses (CRSS) of prismatic, basal, and pyramidal <c+a> slip are important constitutive parameters for the CPFE model. These values were identified by optimizing the CRSS values in simulations of the topographic pile-ups surrounding conical nano-indentations in

### *How would you…*

**…describe the overall significance of this paper?**

*Crystal plasticity finite element constitutive models with phenomenological hardening rules are insufficient to predict the evolution of heterogeneous deformation that precedes damage nucleation near grain boundaries.*

**…describe this work to a materials science and engineering professional with no experience in your technical specialty?**

*The mechanisms that govern dislocation and twin interactions with grain boundaries (slip transfer rules) need to be identified so that models can be developed, implemented, and validated.*

**…describe this work to a layperson?**

*This research program seeks to discover how a crack becomes a crack when there was no crack before. With this knowledge, improvements in material performance can be developed for a wide range of applications.*


Figure 1. A microstructural patch after 1.5% strain. The EBSD map is overlaid on the backscattered electron image. The area characterized by AFM is in the dashed-line box. The region modeled using CPFE is outlined by the solid-line box. The activated deformation systems are identified by trace analysis with colored lines.

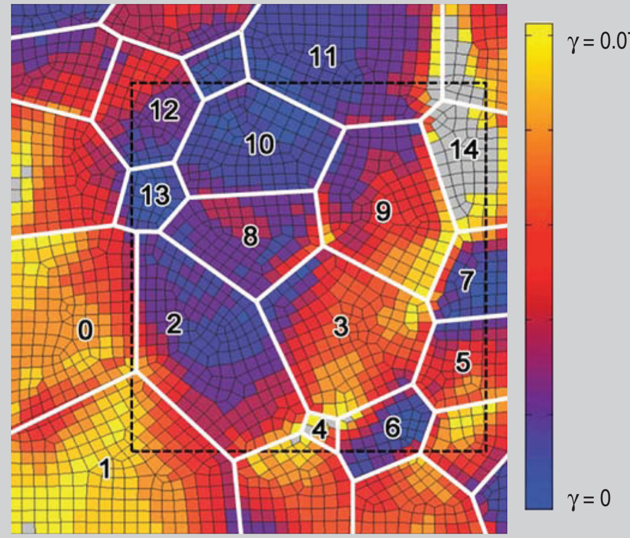


Figure 2. CPFE simulation of the shears developed by all activated deformation systems in the microstructure patch within the solid-line box in Figure 1 at 1.5% global strain.

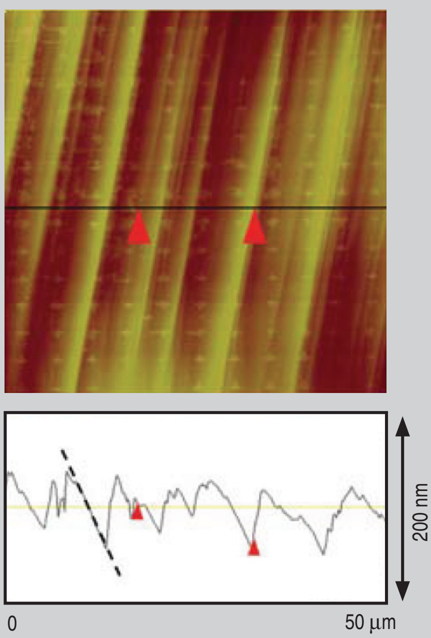


Figure 3. Atomic force microscopy image with a line profile showing topographic details of dislocation slip lines in the middle of grain 3. The dashed line in the profile represents the undistorted surface inclination and serves as the basis for evaluating the overall height change along the section (the marker array was deposited for differential image correlation, but it was too coarse to be useful).

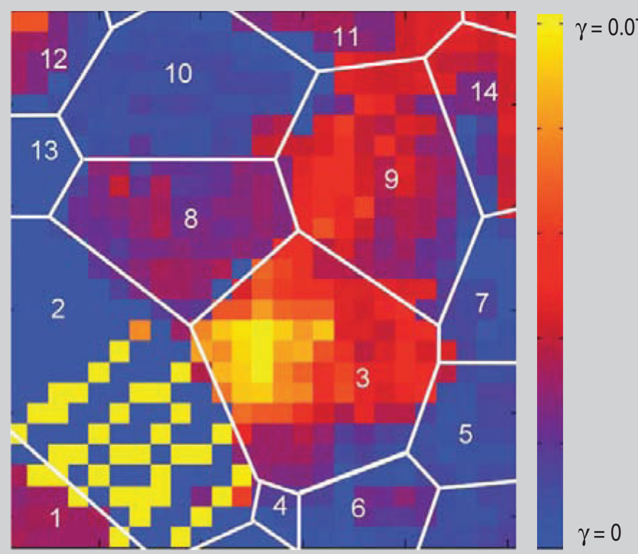


Figure 4. The AFM-based experimentally measured sum of all individual local shear distribution map of the highly characterized microstructure patch shown in Figure 1 at global strain level of 1.5%.

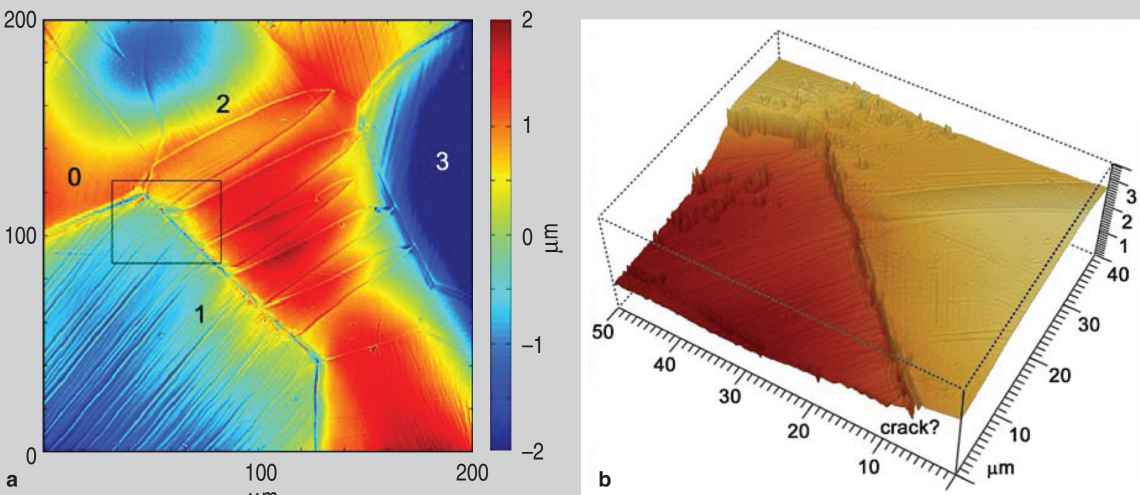


Figure 5. (a) Topographic representation of surface height in grains 1,2,3 using a data set obtained using confocal microscopy. (b) The boundary between grains 1 and 2 suggests that a crack is in the process of forming.

grain interiors using the same phenomenological CPFE model. By comparing experimental results with CPFE simulations from the same grain patches, along with careful study of dislocation interactions at grain boundaries using 3D-XRD, the accuracy of the phenomenological model was assessed. From this, developments required to improve modeling strategies have been identified.

See the sidebar for experimental details.

## DEFORMATION MICROSTRUCTURE

Figure 1 shows a backscattered electron micrograph with a superposed orientation map that illustrates a patch of microstructure after 1.5% plastic strain. Two overlaid frames identify regions that were examined using AFM (dashed lines) and simulated with CPFE (solid line). The free surface topography shows slip traces that vary from grain to grain, due to the differences in crystal orientation (most visible in grains 0, 1, 9; higher resolution images clearly show traces parallel to the colored lines that identify slip traces). The activated deformation systems were identified using trace analysis,[21] based on the backscattered electron (BSE) images and electron backscattered diffraction (EBSD) to determine grain orientation. Prismatic, basal, and pyramidal <c+a> slip, as well as T1 twinning, were found in this patch, as denoted by the trace colors in Figure 1.

## CPFE SIMULATION

The mesh for the CPFE model was generated based on the two-dimensional geometry EBSD map of the undeformed patch. A 3D mesh was generated by extending the two-dimensional geometry into a five-element thick slab, so that the grain boundaries were perpendicular to the surface. A pan-like rim, with an orientation that is at the center of the dominant macro-texture component, provided a somewhat realistic bulk constraint to the modeled region. Deformation was imposed by constraining the left side of the pan to zero displacement, and putting a face load to the right.

The local shear distribution in the microstructure patch from all dislocation slip systems at 1.5% plastic strain is quite heterogeneous, as shown in Figure 2. The CPFE simulations showed that the highest shear occurred in grain 14, caused by prismatic slip. Prism slip was dominant in grains 1, 3, and 9, with the local shear ranging from 0.05 to 0.07. Basal slip was observed in grains 5, 7, and 10, but with smaller magnitudes, from 0.005 to 0.02. No significant pyramidal <c+a> slip occurred in the simulation of this microstructure patch. T1 twinning activity dominated the deformation in the lower part of grain 2.

## EXPERIMENTAL ASSESSMENT

To quantitatively assess the accuracy of the simulation results, comparisons were made with direct experimental measurements of the local shears arising from dislocation activity in the microstructure patch. A technique combining AFM and EBSD-based trace analysis was recently developed to quantitatively measure the local dislocation shear activity associated with activated deformation systems in different grains.[14] Figure 3 displays a high magnification BSE image of an example of dislocation slip lines, as well as an AFM image of the same area measuring the surface height change due to the slip lines.

Based on the measurement of sur-

### EXPERIMENTAL AND ANALYTICAL DETAILS

**Authors' Note:** Certain commercial equipment, instruments, software, or materials are identified in this paper to foster understanding. Such identification does not imply recommendation or endorsement by the National Institute of Standards and Technology, nor does it imply that the materials or equipment identified are necessarily the best available for the purpose.

A four-point bend specimen with dimensions of 25 mm × 3 mm × 2.5 mm was cut 45° from the rolling direction of a commercially pure titanium plate with average grain size of about 80 μm and a moderately strong texture (about 8 times random). X-ray diffraction studies prior to deformation indicate that the grains generally contain a low number of dislocations.[14] The specimen surface was mechanically polished prior to deformation, ending with a 0.05 μm colloidal silica suspension. The specimen was then deformed to surface strain steps of about 1.5%, 3%, and 6%. Regions of interest were located near the center of the sample surfaces, where a continuum finite element method (FEM) stress analysis with isotropic properties showed that the stress state was uniaxial tension.[15] The grain morphology, grain orientations, and deformation slip lines were investigated before and after deformation using a Camscan 44FE scanning election microscope with a TSL/Link electron backscattered diffraction system. Tapping mode atomic force microscopy measurements were conducted using a Dimension 3100 produced by Digital Instruments. A Leica ICM 1000 scanning laser confocal microscope using a 635 nm red laser and 50 nm height increments was used to measure the surface topography after deformation. The 3D-XRD was accomplished using the differential aperture x-ray microscopy facility on beam line 34-ID-E at the Advanced Photon Source at Argonne National Laboratory.

The crystal plasticity constitutive framework is based on a formulation using the multiplicative decomposition of the total deformation gradient and considering the anisotropic elastic constants of α-titanium, which are discussed in detail in References 16–18. The deformation gradient, denoted as **F**, is decomposed into two parts in a finite deformation framework, the elastic, $\mathbf{F}^e$, and plastic ,$\mathbf{F}^p$:, gradients, Equation 1. (All equations are presented in the Equations table.) The evolution of the plastic gradient, $\mathbf{F}^p$, is given by Equation 2, where the plastic velocity gradient, $\mathbf{L}^p$, resulting from activity on all deformation systems is described as Equation 3 with $\mathbf{P}^\alpha = \mathbf{m}^\alpha \otimes \mathbf{n}^\alpha$ as the Schmid matrices with respect to the undeformed state, $\dot{\gamma}_0 = 10^{-3} s^{-1}$ as reference shear rate, $n$ the constant stress exponent, $\tau^\alpha$ the resolved shear stress, and $s^\alpha$ is the shear resistance. The evolution of $s^\alpha$ during deformation is written as Equation 4. The resolved shear stress $\tau^\alpha = \mathbf{P}^\alpha : \mathbf{S}$, where S is the second Piola–Kirchhoff stress $\mathbf{S} = \mathbf{C} : \mathbf{E}^e$. **C** is the fourth order tensor of linear elastic moduli and the elastic strain $\mathbf{E}^e$ is obtained from the elastic deformation gradient as Equation 5, with **I** the second-order identity tensor. The quantities $h_0^\beta$, $a$, and $s_s^\alpha$ are the three hardening parameters. Mechanical twinning was implemented as unidirectional shear with slip resistance properties similar to basal slip. The parameters used were initially chosen from previous studies[18] and then adjusted slightly to obtain better agreement with experimental characterization and to enhance numerical stability. These parameters have been more recently adjusted to include latent hardening and used in conjunction with conical indentation experiments, following the methods described in References 19 and 20. The crystal plasticity formulation was integrated into the commercial FEM system MSC.Marc.

face height change (h), the number of slip/twinning dislocations shearing a given volume of material can be calculated as Equation 6 where $N^{\alpha}$ is the number of dislocations, $\boldsymbol{b}^{\alpha}$ is the Burgers vector of the identified deformation system, α, using trace analysis, and $\boldsymbol{e}_z$ is the normal to the sample surface. The microstructural patch was subdivided into a 25×25 array of 10 μm tiles indicated by indices $m,n$, each of which was scanned by AFM. AFM section lines similar to that shown in Figure 3 were collected along the centerline of each tile, and the local shear ($\gamma^{\alpha}_{mn}$) associated with each deformation system α was calculated as Equation 7 where $\boldsymbol{n}^{\alpha}$ is the plane normal of deformation system α and $\mathbf{X}_{mn}$ is a vector pointing along the scan line with a constant length of 10 μm.

The local shear maps at 1.5% strain generated from AFM data (Figure 4) indicate that the simulation successfully predicted the presence and magnitude of most of the active dislocation slip and twinning systems. The highest shear value in the simulation is about the same as that measured using AFM for most of the grains (2, 3, 6, 8, 9, 10, and 13) in the center of the patch. However, the spatial distribution of simulated local shear is frequently different from the experimental measurement. In grain 3, the CPFE model showed the highest shear in the lower right of grain 14 rather than to the left of center. Also, near the boundary between grains 3 and 8, the shear caused by prismatic slip in grain 3 is about 0.05 to 0.07, which is lower in the simulation. In contrast, the basal shear activity in grains 5 and 7 varied from 0.005 to 0.02, which is modeled accurately in terms of magnitude and distribution. For grain 10, the CPFE simulation successfully captured the basal activity both spatially and quantitatively, but did not predict the pyramidal <c+a> slip activity in the right side of this grain. Since the shear contribution of twinning was only simulated as a homogeneous unidirectional slip system, the localized twins in grain 2 could not be captured properly. Thus, the shears caused by twinning are diffuse rather than spatially concentrated, so the magnitude can only be semi-quantitatively compared to the experiment. Given this, the twin shear was

**Equations**

$$\boldsymbol{F} = \boldsymbol{F}^{e}\boldsymbol{F}^{p} \quad (1)$$

$$\dot{\boldsymbol{F}}^{p} = \boldsymbol{L}^{p}\boldsymbol{F}^{p} \quad (2)$$

$$\boldsymbol{L}^{p} = \sum_{\alpha}^{N_{def.sys.}} \boldsymbol{P}^{\alpha}\dot{\gamma}_0 \left|\frac{\tau^{\alpha}}{s^{\alpha}}\right|^{n} \operatorname{sgn}(\tau^{\alpha}) \quad (3)$$

$$\dot{s}^{\alpha} = \sum_{\beta}^{N_{def.sys.}} h_0^{\beta}\left(1-\frac{s^{\alpha}}{s_s^{\alpha}}\right)^{a}\left|\dot{\gamma}^{\beta}\right| \quad (4)$$

$$\boldsymbol{E}^{e} = \frac{1}{2}\left(\boldsymbol{F}^{eT}\boldsymbol{F}^{e} - \boldsymbol{I}\right) \quad (5)$$

$$N^{\alpha} = \frac{h^{\alpha}}{\boldsymbol{b}^{\alpha}\cdot\boldsymbol{e}_z} \quad (6)$$

$$\gamma^{\alpha}_{mn} = \left(b^{\alpha}N^{\alpha}_{mn}\right)\Big/\left(\boldsymbol{X}_{mn}\cdot\boldsymbol{n}^{\alpha}\right) = \left(\frac{b^{\alpha}\,h_{mn}}{\boldsymbol{b}^{\alpha}\cdot\boldsymbol{e}_z}\right)\Big/\left(\boldsymbol{X}_{mn}\cdot\boldsymbol{n}^{\alpha}\right) \quad (7)$$

distributed in a spatially similar way along the lower left grain boundary, but did not extend into the grain interior.

In a concurrent study, the use of scanning laser confocal microscopy to measure quantities similar to that obtained by AFM is under investigation with characterization following ≈6% global strain. At this strain, the twins grew sufficiently thick to nearly merge with each other on the side next to grain 1, but remained tapered on the side next to grain 3. Figure 5 shows a topographic representation of the neighborhood of grains 1, 2, 3 that indicates how the harder grain 2 resisted deformation (it has the highest topographic elevation) while grains 1 and 3 sunk due to being more highly strained. The twin topography is also evident, as the upper side has a higher elevation than the lower side in each twin. Clearly the influence of deformation in grains 0 and 1 affect deformation in grain 2, as the upper part of grain 2 has a depression that indicates that a greater amount of local strain has occurred. Figure 5b illustrates in higher magnification the region where the twins nucleated at the boundary between grains 1 and 2, which shows an additional depression along the grain boundary that may be the beginning of a crack. Further deformation will be imposed and the continuing evolution of deformation and damage in this region will be reported in a future paper.

## NANO-INDENTATION CHARACTERIZATION AND CPFE PARAMETER OPTIMIZATION

An efficient way to improve the existing CPFE model is to more accurately determine the critical resolved shear stress (CRSS, or $s^{\alpha}$) and hardening parameters of deformation systems using single crystal experiments. However, for hexagonal metals it is difficult to use conventional uniaxial tensile tests of single crystals to measure the CRSS. This is because the wide range of CRSS values for the different deformation system types makes it difficult to isolate specific systems without activating other systems with lower CRSS.

Nano-indentation experiments combined with CPFE simulations provide an alternative opportunity to study the behavior of single crystals in a polycrystalline environment. Because in most cases the grain size is much larger than the size of the indentations, nano-indention can be treated as the deformation of a constrained single crystal. Such experiments allow the separation of the influence of intrinsic grain properties, such as grain orientations, from the influence of polycrystallinity such as interfaces and neighboring grain orientations. A study of the anisotropic nano-indentation response of α-titanium was conducted to quantitatively identify the CRSS for different slip systems.[19,20]

Based on a large-area EBSD scan, a suitable microstructure patch in another specimen from the same plate was chosen to provide a variety of crystallographic orientations for nano-indentation, as shown in Figure 6. These indentations were carried out using a spheroconical diamond tip with a nominal tip radius of 1 μm and a nominal cone angle of 90°. Load-controlled indentations were performed with a maximum load of 6 mN. Residual surface topography of selected indents in the middle of each grain (to avoid grain boundary effects) were measured by AFM. Figure 7a displays the residual pile-up topographies as measured by AFM positioned on an inverse pole figure of the indentation direction. The indentation data and the indent sizes show that the [0001] indentation axis is the hardest direction, as the residual impressions are shallower than in other orientations. For indentation axes away from the [0001] direction, two dominant pile-up hillocks are always formed on opposite sides of the impression. No twins were found in EBSD scans after indentation, and the AFM topographies showed no twin-shaped surface features.

As shown in Figure 7b, corresponding CPFE simulations using a constitutive model similar to that used in the previous section (but with latent hardening included) predicted pile-up patterns in good agreement with the experimental measurements. The CRSS values for prismatic, basal, and pyramidal <c+a> slip of the CPFE model were identified by optimizing the simulation results (load–displacement and residual pile-up pattern) of the indentation process in different grain orientations. Non-linear optimization was conducted by applying a custom implementation of the downhill simplex method after Nelder and Mead.[22,23] The calculated values of CRSS were (150 ± 4) MPa for prismatic slip, (349 ± 10) MPa for basal slip, and (1107 ± 39) MPa for pyramidal <c+a> slip, respectively. The CRSS value for prismatic slip is expected to have better accuracy using this optimization process than the lesser active slip systems. These values imply that basal and <c+a> slip are more difficult to activate than the values used in the prior model, where the ratios used were 1:2:3 for prism:basal:<c+a> CRSS values. However, increasing these ratios resulted in negligible basal and <c+a> slip, which is inconsistent with the experimental observations. Introduction of latent hardening using the 1:2:3 CRSS ratio made only minor differences, indicating that this highly tuned phenomenological model based upon indentation did not significantly improve the simulation. Two possible reasons for the poorer fidelity with experiment are that the loading conditions for indentation contain significant hydrostatic compression, which may affect slip resistance by non-Schmid stress components that affect slip activation.[24] Secondly, the lack of grain boundaries may also frustrate dislocation nucleation processes for non-prism slip.[25] Furthermore, the CPFE simulation does not contain any form of additional slip resistance across a grain boundary.[13] Simulation of the sub-surface grain geometry with an accurate 3D mesh may also positively affect model accuracy. Improvement in modeling slip behavior near grain boundaries appears to be necessary to improve the agreement between experiment and simulation.

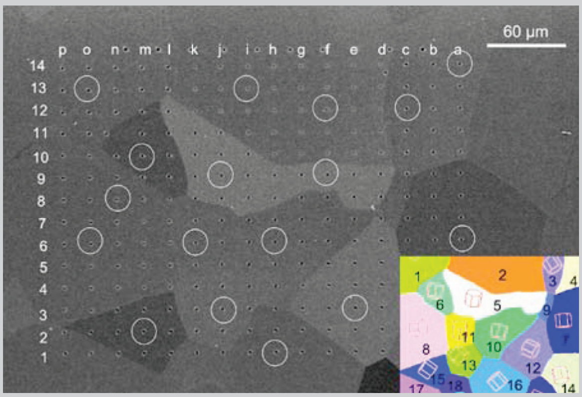


Figure 6. The 20 × 16 μm grid of indents applied on a microstructure patch. Selected indents (highlighted by white circles) in each grain were investigated in detail using AFM and simulated using the CPFE method.

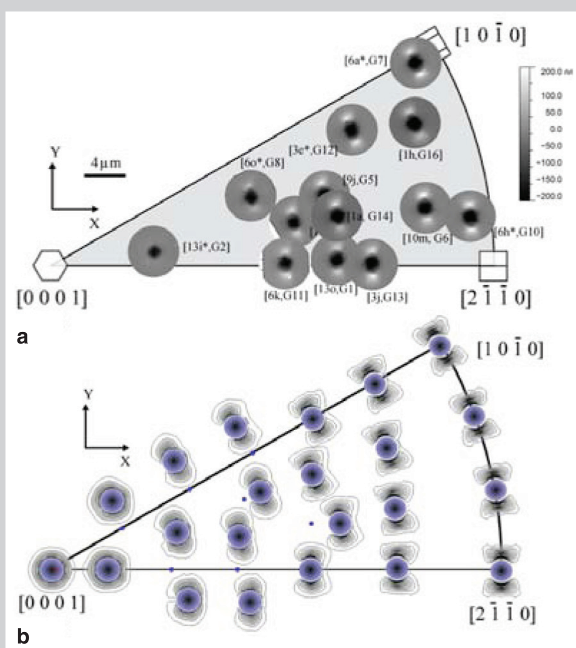


Figure 7. The experimentally measured (a) and CPFE simulated (b) pile-up topography laying on an inverse pole figure of α-titanium according to their indentation axis. In simulation results, regions below the zero level are shown in blue and pile-up is shown in grayscale. Corresponding crystal plasticity finite element simulations predicted the pile-up patterns with good accuracy.

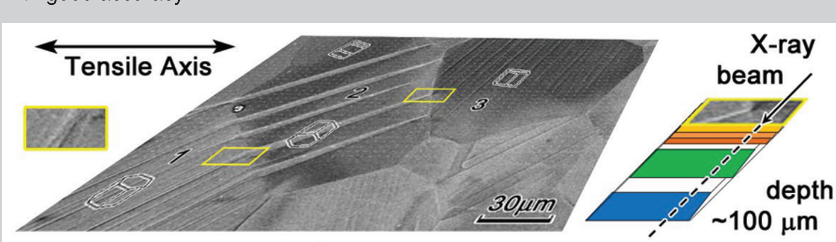


Figure 8. Two DAXM volume scans (20×10 $\mu m^2$, step size = 2 μm) were performed at the boundary between grain 1 and 2, and grain 2 and 3. The scanned regions on the surface are indicated by the two yellow boxes making 2 μm steps with a nominally 1 μm beam. A DAXM volume scan probes a parallelepiped beneath the surface. The microstructure in the 3-D space can be visualized by showing 2D sections of the parallelepiped at different depths.

## SLIP TRANSFER ACROSS GRAIN BOUNDARIES

To better assess how local dislocation content and orientation gradients are affected by grain boundaries, slip transfer phenomena were investigated in this specimen.[26,27] Evidence for slip transfer is apparent in the boundary between grains 1 and 2, where the twin in grain 2 developed due to slip transfer from the active prism slip system in

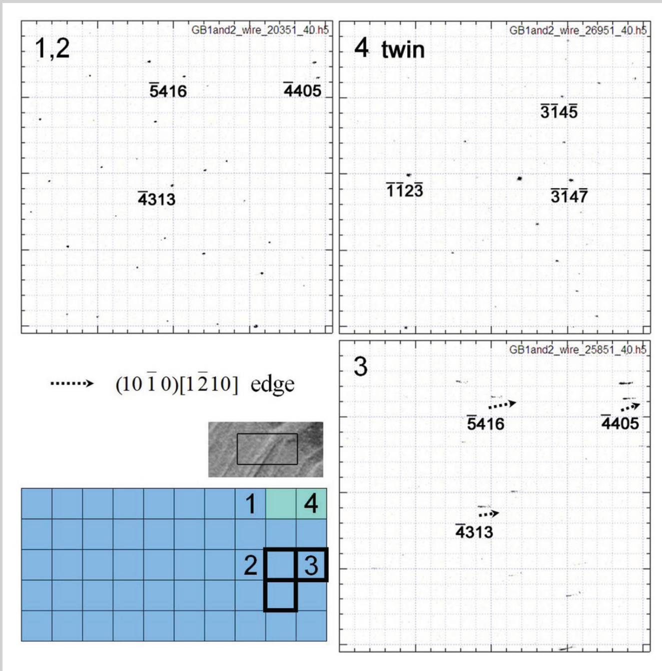


Figure 9. A section of the DAXM volume scan near the boundary between grains 1 and 2 at 2 μm beneath the surface. Grain 1 and the twin are represented by cyan and turquoise color, respectively. The 3 pixels surrounded by thick boxes show moderately streaked peaks, while the other 47 pixels all show sharp peaks. Laue patterns of 4 pixels are shown. In pattern 3, the black dotted arrows near three indexed peaks represent the theoretical peak streak direction caused by $(10\bar{1}0)[1210]$ edge dislocations.

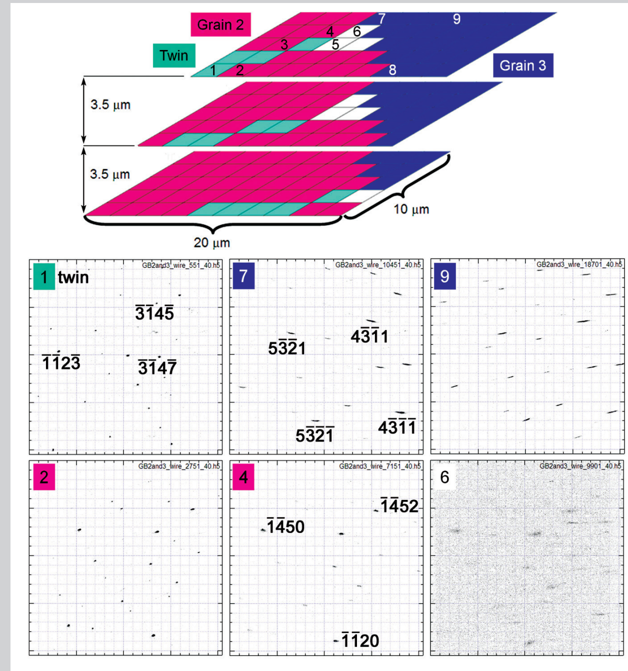


Figure 10. Three sections of the DAXM area scan near the boundary between grains 2 and 3 show how the grain boundary and twin are inclined to the surface. Selected Laue patterns from numbered voxels on the top scan are shown. Laue patterns from grain 3 display significantly streaked peaks. Pattern 6 uses an intensity threshold that is lower than the rest of the patterns to make the peaks more visible.

grain 1. In this case, the geometrical alignment between the prism slip system in grain 1 and the twinning system in grain 2 was quite high. This alignment is described by the slip transfer parameter $m' = \cos\psi \cdot \cos\kappa = 0.94$, where $\psi$ is the angle between the prism slip plane normal in grain 1 and the twinning plane normal in grain 2 and similarly, $\kappa$ is the angle between the prism slip Burgers vector and the twinning Burgers vector. In contrast, slip transfer from the twin system in grain 2 to the active prism slip system in grain 3 has $m' = 0.73$, a significantly lower value. A statistical comparison of 26 boundaries with similar geometrical relationships for active prism slip in one grain and high Schmid factors for twinning (under uniaxial tension) in the neighboring grain showed that only boundaries with $m'$ values > 0.88 exhibited slip transfer. Because two boundaries with $m' > 0.95$ did not show slip transfer stimulated twinning, this parameter is apparently necessary but not sufficient, indicating that local stress tensors must be considered, or additional criteria must be satisfied. An important outcome of this analysis was that the activated twin system only sometimes had the highest Schmid factor (and in a couple of cases the activated twin system had the lowest Schmid factor based upon the global stress state), indicating that nucleation is the critical part of the process for activating mechanical twins (see also Reference 28 for a similar outcome based upon a statistical study, and Reference 29 that shows how dislocations entering a grain boundary can facilitate twin nucleation). These two boundaries were further investigated using 3D differential aperture x-ray microscopy (DAXM[30–32]) to characterize subsurface microstructure and GNDs at two ends of a twin in grain 2 to gain further understanding of slip transfer and the twin nucleation process. Quantified GND content is useful for making detailed comparisons between measured and simulated GND content.

## CHARACTERIZING SUBSURFACE MICRO-STRUCTURE AND GNDS

In DAXM, the polychromatic x-ray beam penetrated the sample 45° from the surface normal in the direction of the tensile axis as illustrated in Figure 8. Scattered photons from a polychromatic beam were captured with an area detector located 90° from the incoming beam above the sample. Scans were made where slip transfer led to twin nucleation, and on the other side of grain 2 where the same twin was stopped by the boundary between grains 2 and 3. Both scans covered a rectangular surface area of (20 x 10) $\mu m^2$, with a step size of 2 μm and the volume in a subsurface parallelepiped about 100 μm deep, which can be visualized as a series of orientation maps beneath the surface.

In Figure 8, the parallelepiped volume of the area scan at the boundary between grains 1 and 2 almost entirely fell into grain 1. Only a few voxels near the upper-right corner of the scanned area show diffraction peaks from the twin. Figure 9 shows a 2D orientation map from about 2 μm beneath the surface. Of the 50 Laue diffraction patterns, all except the upper right two patterns came from grain 1. The Laue patterns of 4 pixels are shown in Figure 9; patterns 1 through 3 are from grain 1, and pattern 4 from the twin. All of the diffraction patterns showed nearly circular (sharp) peaks except for the three locations marked with a box where moderately streaked diffraction patterns were observed. These correspond to regions where the prism slip band was not lined up with a location where slip to twin deformation transfer occurred at the boundary with grain 2 (note inset in Figure 8). These streaked spots are evidence for dislocation pile-ups that cause an accumulation of geometrically necessary dislocations. Using Nye's dislocation tensor, the theoretical peak streak direction can be calculated for any chosen GND population of edge dislocations[13,30–33] and compared with experimental measurements. From such inverse calculations, the peak streak analysis indicates that the GNDs could be caused by prismatic $\{10\bar{1}0\} < 1\bar{2}10 >$ <a> edge dislocations, which is the system responsible for the slip bands in grain 1 (it has a global Schmid factor of 0.478).

The second investigated parallelepiped with Laue patterns from selected voxels of grain 2 (red), grain 3 (blue), and the twin (cyan) are shown in Figure 10. Pattern 1 shows a characteristic diffraction pattern for the twin with slightly elliptical peaks, consistent with the other end of the twin at the boundary between grains 1 and 2, indicating a weak presence of GNDs. The three white voxels ahead of the tip of the twin have Laue patterns with weak, hazy peaks, indicating a severely deformed lattice, but the few recognizable peaks have the same orientations as grain 2. The extreme deformation is probably due to the plastic accommodation where the twin growth interface terminates in the matrix.[34–36] In addition, there is a large shift in peak positions from voxel 2 to voxel 6, which implies the existence of a large orientation gradient in front of the twin tip. In grain 3, the peaks are significantly streaked, and the direction of streaked peaks in patterns 7 and 8 is different from that in pattern 9. Hence, grain 3 has a significant amount of GNDs, and there are at least two types of GNDs present. In the interior of grain 3, at location 9, edge GNDs on the activated prism <a> slip system $\{10\bar{1}0\} < 1\bar{2}10 >$ exist (which has a high global Schmid factor = 0.467). Near the grain boundary, a different slip system must account for the streaked peaks. The strongly streaked patterns indicate a high GND population, that is significant pile-ups of dislocations.

Grains 1 and 3 both displayed active prismatic slip that impacted boundaries with grain 2. However, the density of GNDs in grain 3 was found to be much higher than in grain 1 by comparing the extent of the streak in these two grains. This difference can be accounted for by the slip transfer effect. Near the boundary between grains 1 and 2, prismatic dislocations generated in grain 1 by slip transfer were readily absorbed and transformed into twinning dislocations in grain 2 ($m'$ is 0.94 for this process). This suggests that no significant dislocation pile-up remained in grain 1, resulting in sharp diffraction peaks. The prismatic dislocations generated in grain 3, however, which preceded the twin formation (as the strain caused a greater depression in grain 3 than grain 1 inFigure 5a), were less able to transfer into grain 2, as $m'$ between the twin and the prismatic slip in grain 3 was 0.73, much lower than the average $m'$ value in grain pairs where slip–twin transfer occurred. As slip transfer was not possible, prismatic dislocations piled up at the boundary between grains 3 and 2 and caused lattice curvature (streaked peaks), and activation of at least one other accommodating slip system. The smaller $m'$ can account for the fact that the twin terminated in grain 2 instead of further expanding along the boundary between grains 2 and 3.

Finally, the DAXM technique can be coupled with CPFE modeling, to p rovide a non-destructive assessment of grain boundary inclinations. The DAXM scan at the boundary between grains 2 and 3 shown in Figure 10 shows that it is almost perpendicular to the sample surface. It is possible to compare lattice rotation (peak shift and streaked peaks) measured by DAXM with the calculated rotations from CPFE simulations, which will be examined in future work. From these studies, criteria that describe how dislocations interact with grain boundaries can be developed, which should be implemented into constitutive models used in CPFE simulation.

## CONCLUSIONS

The experimental results indicate that a CPFE model with phenomenological hardening can simulate the heterogeneous deformation process in commercial purity titanium at a level that is roughly consistent with experiments. The spatial distribution of deformation, however, shows some differences from the experimental measurement. Optimized simulation of the nano-indentation process constrained by experimental measurements led to refined constitutive parameters, but use of these parameters did not significantly improve the simulation. The nano-indentation approach evaluated slip behavior in hydrostatic compression states that may not be equivalent to the predominantly tensile stresses present in the bent polycrystalline sample. To further improve the accuracy of CPFE simulation, a deeper understanding of how deformation is influenced at and across grain boundaries needs to be cast into the constitutive description of crystal plasticity.


## ACKNOWLEDGEMENTS

*This research is supported by a Materials World Network grant (NSF DMR-0710570 and DFG EI 681/2-1). Use of the Advanced Photon Source was supported by the U.S. Department of Energy, Office of Science, Office of Basic Energy Sciences, under Contract No. DE-AC02-06CH11357. R.B. is supported by the Materials Sciences and Engineering Division, Office of Basic Energy Sciences, U.S. Department of Energy.*


### References


1. R.A. Lebensohn and C.N. Tome, *Acta Metall. Mater.,* 41 (9) (1993), pp. 2611–2624.
2. Z. Yao and R.H. Wagoner, *Acta Metall. Mater.,* 41 (2) (1993), pp. 451–468.
3. F. Delaire, J.L. Raphanel, and C. Rey, *Acta Mater.,* 48 (5) (2000), pp. 1075–1087.
4. S. Zaefferer, *Mater. Sci. Eng. A,* 344 (2000), pp. 20–30.
5. F. Bridier, P. Villechaise, and J. Mendez, *Acta Mater.,* 53 (2005), pp. 555–567.
6. J.W. Christian and S. Mahajan, *Prog. Mater. Sci.,* 39 (1995), pp. 1–157.
7. F.P.E. Dunne, D. Rugg, and A. Walker, *Int. J. Plasticity,* 23 (2007), pp. 1061–1083.
8. R. Becker and S. Panchanadeeswaran, *Acta Metall. Mater.,* 43 (1995), pp. 2701–2719.
9. D. Raabe, M. Sachtleber, Z. Zhao, F. Roters, and S. Zaefferer, Acta Mater., 49 (2001), pp. 3433–3441.
10. S.R. Kalidindi, A. Bhattacharyya, and R.D. Doherty,

*Proc. R. Soc. Lond.,* 460A (2004), pp. 1935–1956.
11. F. Roters, *Comput. Mater. Sci.,* 32 (2005), p. 509.
12. F. Roters, P. Eisenlohr, L. Hantcherli, D.D. Tjahjanto, T.R. Bieler, and D. Raabe, *Acta Mater.,* 58 (2010), p. 1152.
13. L. Wang, R. Barabash, Y. Yang, T.R. Bieler, M.A. Crimp, P. Eisenlohr, W.J. Liu, and G.E. Ice, *Metall. Mater. Trans. A,* 42A (2011), pp. 626–635.
14. Y. Yang, L. Wang, T.R. Bieler, P. Eisenlohr, and M.A. Crimp, *Met. Mat. Trans.,* 42A (2011), pp. 636–644.
15. B. Wagenknecht, D. Libiran, S. Poon, and K. Sztykiel, "In-Situ Four-Point Bending Apparatus for Scanning Electron Micro- scopes" (Senior Design Project, Mechanical Engineering, Michigan State University, Apr. 2008).
16. S.R. Kalidindi, C.A. Bronkhorst, and L. Anand, *J. Mech. Phys. Solids,* 40 (1992), pp. 537–569.
17. S.R. Kalidindi and L. Anand, *Metall. Trans. A,* 24A (1993), pp. 989–992.
18. A.A. Salem, S.R. Kalidindi, and S.L. Semiatin, *Acta Materialia,* 53 (2005), pp. 3495–3502.
19. C. Zambaldi and D. Raabe, *Acta Mater.,* 58 (2010), p. 3516.
20. C. Zambaldi, Y. Yang. T.R. Bieler, and D. Raabe, *J. Mater. Res.,* (accepted for 2012 publication).
21. B.A. Simkin, B.C. Ng, T.R. Bieler, M.A. Crimp, and D.E. Mason, *Intermetallics,* 11 (2003), pp. 215–223.
22. J. Nelder and R. Mead, *Computer Journal,* 7 (1965), p. 308.
23. W. Press, S. Teukolsky, W. Vetterling, and B. Flannery, *Numerical Recipes C++* (Cambridge, U.K.: Cambridge University Press, 2007).
24. V. Vitek, A. Mrovec, R. Groger, J.L. Bassani, V. Racherla, and L. Yin, *Mater. Sci. and Eng.,* A-387 (2004), pp. 138–142.
25. M.A. Tschopp, D.E. Spearot, and D.L. McDowell, *Dislocations in Solids,* Vol. 14, ed. J.P. Hirth (Cambridge, MA: Elsevier Publishers, 2008), pp. 43–140.
26. L. Wang, Y. Yang, P. Eisenlohr, T.R. Bieler, M.A. Crimp, and D.E. Mason, *Metall. Mater. Trans. A,* 41 (2010), pp. 421–430.
27. L. Wang, P. Eisenlohr, Y. Yang, T.R. Bieler, and M.A. Crimp, *Scripta Materialia,* 63 (2010), pp. 827–830.
28. I.J. Beyerlein, L. Capolungo, P.E. Marshall, R.J. McCabe, and C.N. Tome, *Philosophical Magazine,* 90 (2010), pp. 2161–2190.
29. J. Wang, R.G. Hoagland, J.P. Hirth, L. Capolungo, I.J. Beyerlein, and C.N. Tomé, *Scripta Materialia,* 61 (2009b), pp. 903–906.
30. R. Barabash, G. Ice, B. Larson, G.M. Pharr, K.-S. Chung, and W. Yang, *Appl. Phys. Letters*, 79 (2001), pp. 749–751.
31. W. Liu, G.E. Ice, B.C. Larsen, W. Yang, and J.Z. Tischler, *Ultramicroscopy,* 103 (2005), pp. 199–204.
32. R.I. Barabash, G.E. Ice, M. Kumar, J. Ilavsky, and J. Belak, *Int. J. Plast.,* 25 (2009), pp. 2081–2093.
33. L. Wang, "Evolution of Deformation Twins and Dislocation Near Grain Boundaries in Commercial Purity Titanium" (Ph.D. Dissertation, Michigan State University, 2011).
34. A.W. Sleeswyk, *Acta Metallurgica,* 10 (1962), pp. 705–725.
35. S. Mahajan and G.Y. Chin, *Acta Metallurgica,* 22 (1974), pp. 1113–1119.
36. S. Vaidya and S. Mahajan, *Acta Metallurgica,* 28 (1980), pp. 1123–1131.

**Y. Yang, L. Wang, M.A. Crimp, and T.R. Bieler are with the Department of Chemical Engineering and Materials Science, Michigan State University, East Lansing, MI 48824; P. Eisenlohr and C. Zambaldi are with the Max-Planck-Institut für Eisenforschung, Düsseldorf, Germany; R.I. Barabash is with Oak Ridge National Laboratory, Oak Ridge, TN; W. Liu is with Advanced Photon Source at Argonne National Laboratory, Argonne, IL; M.R. Stoudt is with the National Institute of Standards, Gaithersburg, MD. Prof. Bieler can be reached at bieler@egr.msu.edu.**



**Li** *(Continued from page 65.)*

*synthesis.*

## References

1. J.W. Christian and S. Mahajan, *Prog. Mater. Sci.,* 39 (1995), p. 1.
2. L. Lu, X. Chen, X. Huang, and K. Lu, *Science,* 323 (2009), p. 607.
3. Lei Lu, Yongfeng Shen, Xianhua Chen, Lihua Qian, and K. Lu, *Science,* 304 (2004), p. 422.
4. E. Ma, M. Wang, QH. Lu, M.L. Sui, L. Lu, and K. Lu, *Appl. Phys. Lett.,* 85 (2004), p. 4932.
5. X.Y. Li, Yujie Wei, Lei Lu, Ke Lu, and Huajian Gao, *Nature,* 464 (2010), p. 877.
6. T. Zhu and Ju Li, *Prog. Mater. Sci.,* 55 (2010), p. 710.
7. X. Zhang, H. Wang, X.H. Chen, L. Lu, K. Lu, R.G.Hoagland, and A. Misra, *Appl. Phys. Lett.,* 88 (2006), p. 173116.
8. O. Anderoglu, A. Misra, H. Wang, and X. Zhang, *J. Appl. Phys.,* 103 (2008), p. 094322.
9. X. Zhang, A. Misra, H. Wang, J.G. Swadener, A.L. Lima, M.F. Hundley, and R.G. Hoagland, *Appl. Phys. Lett.,* 87 (2005), p. 233116.
10. M. Dao, L. Lu, Y.F. Shen, and S. Suresh, *Acta Mater.,* 54 (2006), p. 5421.
11. O. Anderoglu, A. Misra, H. Wang, F. Ronning, M.F.Hundley, and X. Zhang, *Appl. Phys. Lett.,* 93 (2008), p. 083108.
12. X. Zhang, O. Anderoglu, R.G.Hoagland, and A. Misra, *JOM,* 60 (9) (2008), p. 75.
13. C.J. Shute, B.D. Myers, S. Xie, S.-Y. Li, T.W. Barbee, Jr., A.M. Hodge, J.R. Weertman, *Acta Mater.,* 59 (2011), p. 4569.
14. V. Yamakov, , D. Wolf, S. R. Phillpot, A. K. Mukherjee, and H. Gleiter, *Nature Mater.,* 3 (2004), p. 43.
15. V. Yamakov, D. Wolf, S.R. Phillpot, and H. Gleiter, *Acta Mater.,* 50 (2002), p. 5005.
16. K.S. KumarH. Van Swygenhoven, and S. Suresh, *Acta Mater.,* 51 (2003), p. 5743.
17. H. van Swygenhoven, P.M. Derlet, and A.G. Frøseth, *Nature Mater.,* 3 (2004), p. 399.
18. O. Anderoglu, A. Misra, J. Wang, R.G. Hoagland, J.P. Hirth, and X. Zhang, *Int. J. Plast.,* 26 (2010), p. 875.
19. J. Wang and Hanchen Huang, *Appl. Phys. Lett.,* 88 (2006), p. 203112.
20. Ting Zhu, Ju Li, Amit Samanta, Hyoung Gyu Kim, and Subra Suresh, *Proc. Natl. Acad. Sci. U.S.A.,* 104 (2007), p. 3031.
21. K.A. Afanasyev and F. Sansoz, *Nano Lett.,* 7 (2007), p. 2056.
22. Z.-H. Jin, P. Gumbsch, K. Albe, E. Ma, K. Lu, H. Gleiter, and H. Hahn, *Acta Mater.,* 56 (2008), p. 1126.
23. T.C. Lee, I.M. Robertson, and H.K. Birnbaum, *Philos. Mag. A,* 62 (1990), p. 131.
24. T.C. Lee, I.M. Robertson, and H.K. Birnbaum, *Metall. Trans. A,* 21A (1990), p. 2437.
25. Y.B. Wang and M.L. Sui, *Appl. Phys. Lett.,* 94 (2009), p. 021909.
26. J.K. Rittner, D.N. Seidman, and K.L. Merkle, *Phys. Rev. B,* 53 (1996), p. R4241.
27. G. Lucadamo and D.L. Medlin, *Science,* 300 (2003), p. 1272.
28. D.L. Medlin, G.H. Campbell, and C.B. Carter., *Acta Mater.,* 46 (1998), p. 5135.
29. J.A. Brown and N.M. Ghoniem, *Acta Mater.,* 57 (2009), p. 4454.
30. J. Wang, O. Anderoglu, J.P. Hirth, A. Misra, and X. Zhang, *Appl. Phys. Lett.,* 95 (2009), p. 021908.
31. J. Wang, N. Li, O. Anderoglu, X. Zhang, A. Misra, J.Y. Huang, and J.P. Hirth, *Acta Mater.,* 58 (2010), p. 2262.
32. N. Li, J. Wang, J.Y. Huang, A. Misra, and X. Zhang, *Scripta Mater.,* 64 (2011), p. 149.
33. J. Wang, A. Misra, and J.P. Hirth, *Phys. Rev. B,* 83 (2011), p. 064106.
34. L. Liu, J. Wang, S.K. Gong, and S.X. Mao, *Phys. Rev. Lett.,* 106 (2011), p.175504.
35. X.L. Wu, X.Z. Liao, S.G. Srinivasan, F. Zhou, E.J. Lavernia, R.Z. Valiev, and Y.T. Zhu, *Phys. Rev. Lett.,* 100 (2008), p. 095701.
36. N. Li, J. Wang, A. Misra, J.Y. Huang, and J.P. Hirth, *Acta Mater.,* 59 (2011), p. 5989.
37. J.P. Hirth and J. Lothe, *Theory of Dislocations* (New York: Wiley, 1982).
38. C.H. Henager, R.J. Kurtz, and R.G. Hoagland, *Philos. Mag.,* 84 (2004), p. 2277.
39. A. Misra, J.P. Hirth, R.G. Hoagland, J.D. Embury, and H. Kung, *Acta Mater.,* 52 (2004), p. 2387.

**N. Li, J. Wang, and A. Misra are with Los Alamos National Laboratory, Los Alamos, NM 87545, USA; X. Zhang is with the Department of Mechanical Engineering, Materials Science and Engineering Program, Texas A&M University, College Station, TX 77843-3123, USA. Dr. Li can be reached at nanli@lanl.gov.**